A porphyrin spin qubit and its 2D framework nanosheets

Ainhoa Urtizberea, Eva Natividad, Pablo J. Alonso, Miguel A. Andrés, Ignacio Gascón, Michel Goldmann and Olivier Roubeau**

Dr. A. Urtizberea, Dr. E. Natividad, Dr. P. J. Alonso, Dr. O. Roubeau
Instituto de Ciencia de Materiales de Aragón (ICMA), CSIC and Universidad de Zaragoza, Zaragoza, 50009, Spain
E-mail: roubeau@unizar.es

Dr. A. Urtizberea
Centro Universitario de la Defensa, Zaragoza, 50090, Spain
E-mail: ainhoa@unizar.es

Mr. M. A. Andrés, Dr. I. Gascón
Instituto de Nanociencia de Aragón (INA), Universidad de Zaragoza, Zaragoza, 50018, Spain

Dr. M. Goldmann
Sorbonne Universités, UPMC Univ. Paris 06, CNRS-UMR 7588, Institut des NanoSciences de Paris, F-75005 Paris, France

Dr. M. Goldmann
Faculté des Sciences Fondamentales et Biomédicales, Université Paris Descartes, 75006 Paris, France

Dr. M. Goldmann
Synchrotron SOLEIL, L'Orme des Merisiers, Saint-Aubin, BP 48, 91192 Gif-sur-Yvettes, France

Dr. A. Urtizberea, Dr. P. J. Alonso, Dr. O. Roubeau
Departamento de Física de la Materia Condensada, Universidad de Zaragoza, Zaragoza, 50009, Spain

Mr. M. A. Andrés, Dr. I. Gascón
Departamento de Química Física, Universidad de Zaragoza, Zaragoza, 50009, Spain

Keywords: Metal-Organic Frameworks, Magnetic Materials, Thin Films, Porphyrin, Spin Relaxation

Abstract

Molecular spin qubits have been shown to reach sufficiently long quantum coherence times to envision their use as hardware in quantum processors. These will however require their

implementation in hybrid solid-state devices for which the controlled localization and homogeneous orientation of the molecular qubits will be necessary. An alternative to isolated molecules that could ensure these key aspects is 2D frameworks in which the qubit would act as node. In this work, we demonstrate that the isolated metalloporphyrin [Cu(H_4TCPP)] molecule is a potential spin qubit, and maintains similar quantum coherence as node in a 2D [{CuTCPP}$Zn_2(H_2O)_2$] metal-organic framework. Mono- and multi-layer deposits of nanosheets of a similar 2D framework are then successfully formed following a modular method based on Langmuir-Schaefer conditions. The orientation of the {CuTCPP} qubit nodes in these nanosheets is homogeneous parallel to the substrate. These nanosheets are also formed with a control over the qubit concentration, i.e. by dilution with the un-metallated porphyrin. Eventually, 2D nanosheets are formed in-situ directly on a substrate, through a simple protocol devised to reproduce the Langmuir-Schaefer conditions locally. Altogether these studies show that 2D spin qubit frameworks are ideal components to develop a hybrid quantum computing architecture.

1. Introduction

Research towards the development of quantum information has mainly focused on finding and improving the adequate schemes to embody the hardware of this fascinating branch of science.[1] Among these, molecular candidates for quantum bits (qubits) and gates first arose in the form of purely organic systems, using either the multiple nuclear spins of rationally selected molecules or the electronic spin(s) of open shell organic molecules bearing one or multiple radicals. The careful design and selection of such organic molecules coupled to sophisticated experiments have allowed implementing realistic quantum operations using ensembles of these.[2] Paramagnetic coordination complexes were later proposed as alternative molecular spin qubits, after it was argued and shown that the molecule electronic spin orientation and quantum superpositions allow to encode quantum bit (qubit) states.[3] Recent

improvements in the coherence times of these molecular spin qubits[4] and the unique ability to design molecules with multiple qubits as prototypes of quantum gates[5] have brought this scheme to a point where it becomes reasonable to envision the design of a magnetic quantum processor. A magnetic molecule has even recently been used to implement Grover's quantum algorithm, albeit using its metal ion nuclear spin.[6] One of the advantages of the molecular scheme is that macroscopic numbers of identical qubits are obtained in one sole reaction. While this is appealing for the daunting challenge of scaling to a usable size, common to all proposed schemes,[7] the technology to build a *scalable* quantum architecture based on molecular qubits is not yet available. We have nonetheless recently proposed and evaluated the feasibility of hybrid devices in which molecular qubits would be integrated at constrictions along superconducting coplanar resonators.[8] For this proposal to work, two compulsory requirements are i) that only one molecular qubit be coupled to each constriction and ii) that the strong coupling regime be reached (see Fig. 1). The latter is in itself a challenge but calculations and experiments indicate that this could be attainable[8,9] by optimizing the constriction size, the qubit coherence times and obviously the integration of the molecules on the constriction surface itself. Another aspect of relevance for this integration is that the energy gaps and couplings of all qubits should not differ significantly over the whole device. This implies that in addition to being chemically identical, each qubit molecule has to maintain a similar, preferred orientation with respect to the constriction surface.

Research dealing with molecular nanomagnets on surfaces[10] has shown that the integration of molecular qubits as isolated molecules on surfaces would be feasible but that the control of their surface density, i.e. the number of qubit per constriction in our hybrid architecture, and orientation would be difficult.[11,12] A valid alternative to using isolated molecules lies in domains of extended 2D frameworks in which the molecular qubit would act as node.[8] Indeed, the subjacent network periodicity would enforce naturally the strict identity and

homogeneous orientation of all molecules/nodes, while the necessary control on the number of qubits per surface area could be attained by a proper control of dilution with a non-magnetic analogue node. The relative inertness of a network with respect to an isolated molecule may also prove relevant for the robustness of hybrid solid-state devices. To build such 2D networks, porphyrin analogues to the Cu(II) phtalocyanines for which relatively long coherence times have been observed[4d,13] appear as good candidates for the qubit nodes. Indeed, a large number of extended networks are known that form using metal(II) porphyrin molecules bearing four coordinating substituents such as carboxyphenyl or pyridine in combination with metal ions.[14] These are mostly 3D networks in which 2D planes of metal(II) porphyrin are pillared in different ways. There are however a few systems that do present a 2D structure with unpillared planes.[15] For one of these, ultra-thin sheets of few such planes were even produced using a surfactant-assisted synthesis.[16] More interestingly, similar 2D structures have been formed at the air-water interface and deposited on substrates with a variable number of 2D layers by a sequential procedure.[17] In brief, the 2D assembly process uses coordination of the carboxylic acid groups of 5,10,15,20-tetrakis(4-carboxyphenyl)-porphyrin (H_6TCPP, either as free-base or as its [Co(H_4TCPP)] complex), spread over an aqueous subphase, with metal ions of the subphase forming $M_2(COO)_4$ paddle-wheel nodes. The coordination network growth occurs over the liquid surface and is thus forced into a 2D topology, allowing the formation of highly crystalline 2D monolayers.[18,19] These were shown to form very fast as domains of sizes in the range 10-140 nm.[18,19] Transfer to a substrate is carried out by horizontal dipping after compressing these pre-formed domains, and multi-layer structures can be formed by sequential cycles, generating stacks of the 2D frameworks. The advantages of this method for our objectives are the robustness of the metalloporphyrin core, the coherence of bulk deposits in terms of structural phase and 2D layer domains, and their demonstrated stability.[17b] Interestingly, the method has also been successfully extended to [Pd(H_4TCPP)],[18] as well as to ditopic and extended analogues of H_6TCPP.[20] Nonetheless,

this research has mainly been aimed at crystal engineering goals, and so far only paramagnetic Cu(II) ions have been used for the paddle-wheel node connecting the metalloporphyrin units. In this work, we aim to evaluate the adequateness of similar metalloporphyrin 2D frameworks for their implementation as monolayer of 2D networks of spin qubits, using [Cu(H_4TCPP)] and Zn(II) ions as respectively potential qubit and diamagnetic nodes (Fig. 1). Thus, this work first reports the synthesis, x-ray structure and magnetic properties of 2[Cu(H_4TCPP)]·4.5DMF·1.5H_2O (**1**) and its 2D metal-organic framework (MOF) [{CuTCPP}$Zn_2(H_2O)_2]_\infty$·2DMF (**2**). This allows to demonstrate the potential of the isolated [Cu(H_4TCPP)] molecule as spin qubit, as well as to confirm it maintains similar quantum coherence in its 2D framework. We then adapt the Langmuir-Schaefer procedure mentioned above to successfully form mono- and multi-layer deposits of a similar 2D [{CuTCPP}Zn_2] framework. We also show the ability to form these same deposits with a control over the qubit concentration, e.g. by dilution. Eventually, we demonstrate that isolated 2D nanosheets can be formed in-situ directly on a substrate, thereby opening their implementation at specific localizations on a hybrid device.

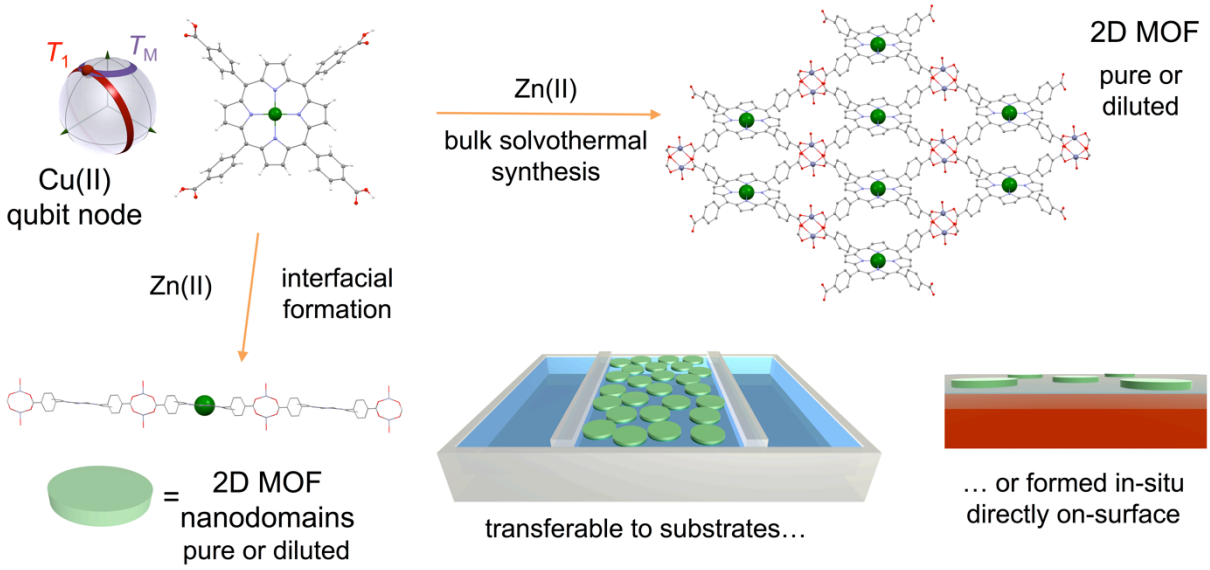

Figure 1. Schematic representation of the elaboration of 2D MOFs built on a Cu(II) porphyrin qubit, either as a bulk solid (top) or 2D nanodomains formed interfacially on a Langmuir trough or directly on a substrate (bottom). The bulk synthesis (top) involves solvothermal reaction in DMF with Zn(II) ions resulting in a pillarless 2D MOF structure built on

tetracarboxylate paddlewheels. Reaction with a mixture of free-base and metallated porphyrin allows to form magnetically diluted analogues. Interfacial synthesis (bottom) involves spreading a porphyrin solution on an aqueous solution containing Zn(II) ions resulting in the fast formation of crystalline 2D nanodomains with a similar topology as the bulk material. These nanosheets are formed on a Langmuir trough for their transfer onto various substrates through Langmuir-Schaeffer procedure or directly on a thin aqueous layer covering a mica surface.

2. Results and discussion

2.1 Synthesis and structures of the qubit node and its 2D MOF

The isolated qubit candidate **1** is obtained by reaction of copper acetate and H_6TCPP in DMF and crystallizes as shiny purple thin plates from the workup DMF:H_2O solution. Indication of the successful metallation of the porphyrin is found in the FT-IR spectrum, with the disappearance of the $\nu_{N–H}$ and $\delta_{N–H}$ bands, respectively at 3309 and 963 cm^{-1} in the free-base H_6TCPP (Fig. S1). Modifications of the spectrum in the C=O and C–OH stretchings and appearance of a band typical of aliphatic $\nu_{C–H}$ at 2926 cm^{-1} also point at the incorporation of DMF, in agreement with the crystal structure (see below). The MALDI-TOF-MS spectra of crystals dissolved in MeOH (matrix: CHCA and DIT, Fig. S3) exhibit the expected molecular peak at m/z = 851, thus showing the [Cu(H_4TCPP)] molecule is stable in the conditions used for the formation of Langmuir films and frozen-solution EPR. UV-Vis absorption spectrum (Fig. S4) confirms these observations, with the Soret band at 416.4 nm, shifted by *ca.* 3 nm with respect to the free-base H_6TCPP, and the observation of one main Q-band at 539.6 and a second much weaker band at *ca.* 577 nm, typical of absorption spectra of Cu(II) porphyrins. The 2D framework **2** was formed by reacting the pre-formed [Cu(H_4TCPP)] with zinc nitrate under autogeneous pressure in DMF, thus using conditions similar to those used to obtain many 3D frameworks,[14] albeit without any pillaring co-ligand. Tiny block purple crystals of the targeted MOF 2 with formula $[\{Cu(TCPP)\}Zn_2(H_2O)_2]_\infty$ were obtained in high yield. A similar procedure was previously used with free-base H_6TCPP and an excess of the zinc salt, resulting in the formation of two polymorphs of $[\{Zn(TCPP)(H_2O)\}Zn_2(H_2O)_2]_\infty$ MOF (coined respectively PPF-1 and BNAS-11).[15b,c] For EPR experiments, magnetically-diluted

analogue $\mathbf{2_{1\%}}$ was prepared using the same procedure and isolated as a polycrystalline powder. The IR spectra of the two materials are virtually identical (Fig. S2) and confirm the carboxylic groups are now deprotonated and participate in coordination bonds. The absence of the δ_{N-H} band in the spectrum of $\mathbf{2_{1\%}}$ and metal content analysis confirm the assumption that all porphyrins are metallated and the formulation $[\{CuTCPP\}_{0.01}\{Zn(H_2O)TCPP\}_{0.99}Zn_2(H_2O)_2]_\infty$.

Compound **1** crystallizes in the triclinic *P*–1 space group (Table S1) as a solvate with formula $2[Cu(H_4TCPP)]\cdot 4.5DMF\cdot 1.5H_2O$. The structure consists of three crystallographically distinct neutral $[Cu(H_4TCPP)]$ molecules, one in general position, [Cu1], and the other two having their central Cu site on an inversion center, [Cu2] and [Cu3], as well as lattice DMF and water molecules. All three Cu(II) ions reside at the center of the porphyrin macrocycle and exhibit a close to square planar geometry with no axial ligand (Fig. 2A and 2B). The two molecules sitting on an inversion center are very similar and show only very little distortion of both the Cu(II) square-planar coordination sphere and the porphyrin macrocycle. Their Cu–N bonds are homogeneous at 1.998(8)/2.002(7) and 1.991(6)/1.996(5) respectively for [Cu2] and [Cu3], while the *cis* N–Cu–N angles are all very close to 90º (Table S2). For both, the pyrrole N atoms and the Cu site pertain to the same plane, the largest displacement of the porphyrin macrocycle off this plane being only 0.138 Å ([Cu2]) and 0.135 Å ([Cu3]), in both cases for one of the external pyrrole carbons. The dihedral angles between neighboring pyrrole rings is only 5.34º/4.04º respectively for [Cu2]/[Cu3] (Table S3). The Cu-porphyrin core in both these molecules is therefore basically undistorted and flat. On the contrary, the porphyrin macrocycle of the molecule in general position, [Cu1], exhibits some appreciable saddle-distortion, with its pyrrole rings pointing alternatively upward and downward out of the N_4 plane. The pyrrole N atoms are ±0.084 Å off their mean plane while the maximal displacements of the pyrrole external carbons out of this mean N_4 plane are in the range 0.383-0.556 Å. Neighboring pyrrole rings form dihedral angles in the range 11.54-14.93º.

Meanwhile, the distortion at the Cu site is in comparison rather limited. Indeed, Cu1 is only 0.014 Å out of the N_4 plane, while the Cu–N bond lengths remain rather similar and the *cis* N–Cu–N angles are still very close to 90º (Table S2). A further difference between the saddled and symmetric molecules lies in the orientation of the two pairs of phenyl rings pointing out of the macrocycle mean plane, respectively towards the same side or opposite sides (Fig. 2B). The lattice DMF and water molecules form hydrogen bonds both with each other and the [Cu(H_4TCPP)] molecules (Table S3), but do not participate in any network connecting the different [Cu(H_4TCPP)] molecules. In the packing, the [Cu1] and [Cu2] molecules form 1D stacks running approximately along the *a* axis (Fig. 2C and D, angle between mean N4 planes = 17.31º, Cu1···Cu2 and Cu1···Cu1 separations of 6.32 and 4.92 Å), which are maintained by intermolecular C–H···π interactions (Fig. S6). In addition, these 1D stacks are also maintained through interactions with the third molecule [Cu3], in the form of stacked phenyl and carboxylic group π clouds from the three molecules (Fig. S7 and 2C). Besides, the 1D stacks are also connected with each other through double H-bonds between carboxylic groups of the [Cu1] and [Cu2] molecules (Fig. 2D, inter-stack Cu1···Cu2 separation of 22.04 Å).

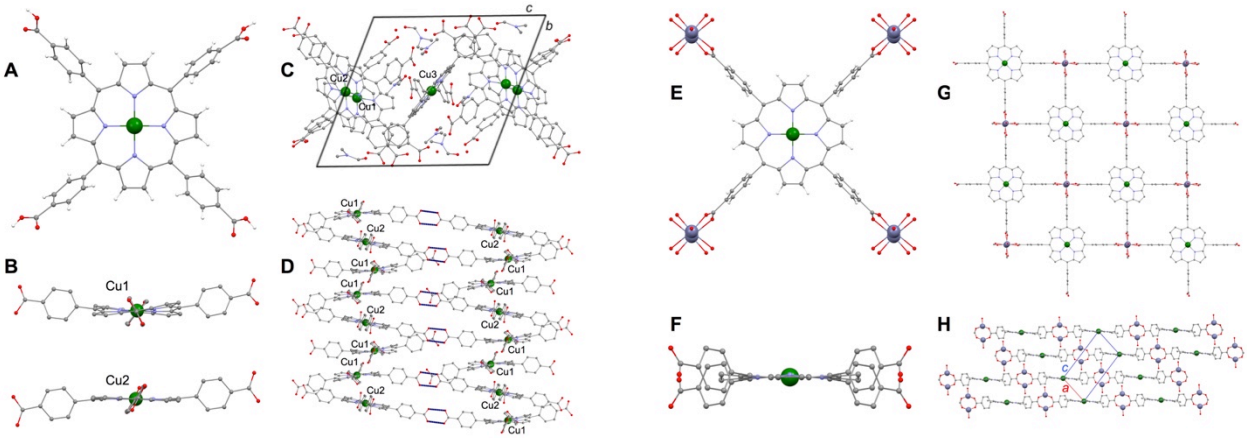

Figure 2: Views of the solid-state structure of **1** (left) and **2** (right): A) face-on view of one ([Cu1]) of the three [Cu(H_4TCPP)] molecules; B) edge-one view of two of the three [Cu(H_4TCPP)] molecules showing the stronger saddle distortion of one of them ([Cu1], top; [Cu2] bottom, [Cu3] being very similar to [Cu2]); C) view along the *a* axis showing the 1D stacks formed by [Cu1] and [Cu2] molecules and their interactions with the [Cu3] molecule;

D) lateral view of the 1D stacks formed by [Cu1] and [Cu2] molecules and their interactions through double H-bonds of their carboxylic acid groups. Note that only one every two Cu1 molecule is involved in these inter-stack H-bonding. E) face-on view of the {Cu(TCPP)} node connected to four [Zn_2] paddle-wheel connecting units; F) edge-one view of the {Cu(TCPP)} node; G) view of the 2D square grids, the Cu···Cu diagonal corresponding to the *b* axis; H) stacking of the 2D planes viewed along the *b* axis. For clarity, hydrogens are only shown in A and E. Color code: Cu, green; Zn, light violet; O, red; N, light blue, C, grey; H, white.

The 2D framework **2** crystallizes in the monoclinic *P*2/m space group as [{Cu(TCPP)}$Zn_2(H_2O)_2]_\infty$·2DMF. The structure is built by {Cu(TCPP)} units connected through $Zn_2(COO)_4$ paddle-wheels, forming neutral 2D square grids parallel to the *b* axis (Fig. 2E, F and G). The grid diagonal distances corresponding to the Cu···Cu and in-plane [Zn_2]···[Zn_2] shortest separations are respectively 16.689 Å (the *b* axis) and 16.567 Å. These grids are stack-shifted along the *a* axis (Fig. 2H), resulting in an inter-plane separation of 4.986 Å, and shortest Cu···Cu separation of 6.655 Å (the *a* axis). The most significant inter-plane interaction arises from the H-bond between the H_2O molecule completing the square-pyramidal environment of the Zn(II) ions and the closest carboxylic oxygen of the neighboring planes, the O3···O1 separation being 3.21 Å (Fig. S8). The plane thickness can be estimated as *ca.* 6.3 Å through the separation between the axial water molecules on the [Zn_2] paddle-wheel. Because the Cu(II) ion occupies a 2/m special position, by symmetry it lies in the porphyrin N_4 macrocyle plane and the only deviation from perfect square-planar environment comes from the slightly different Cu–N bond distances at 1.94(6) Å and 1.96(7) Å, respectively for N1 and N2 sites. The porphyrin ring system is essentially flat (Fig. 2F) with the maximal displacements of the pyrrole external carbons out of the N_4 plane at 0.261 Å and pyrrole-pyrrole dihedral angle of 8.15º. The carboxyphenyl rings are tilted with respect to the porphyrin plane by 83.0º, being nearly perpendicular to the layers (Fig. 2G).

Overall, the {Cu(TCPP)} unit in **2** is extremely similar to the [Cu(H_4TCPP)] moieties in **1**, in particular the Cu(II) ion environment, while the 2D sheets are comparable with those built on {Zn(TCPP)(H_2O)} in PPF-1 and BNAS-11.[15b,c] The main differences with these related 2D

materials are found in the stacking of the planes. In PPF-1, adjacent layers are stacked in an AB pattern with an interlayer separation of 8.747 Å, and the porphyrin Zn site on top of the [Zn_2] paddle-wheel, by symmetry.[15b] In BNAS-11, bilayers are formed by weak interactions with an interlayer separation of 7.835 Å and a similar stack-shift as in **2**.[15c] These bilayers stack in an (AB)(AB) pattern, with a bilayer separation of 8.904 Å, and the porphyrin Zn site on top of the nearest [Zn_2] paddle-wheel from adjacent bilayer. The stacking motif in **2** is thus the most efficient, with a unique interlayer separation, 4.986 Å, significantly shorter. This is most likely related to the absence of axial ligand at the {Cu(TCPP)} unit and the fact the Cu(II) ion lies within the porphyrin plane, contrary to what is observed in the related materials PPF-1 and BNAS-11 in which the Zn(II) lies out of the porphyrin plane and is axially coordinated by a water molecule.[15b,c] These differences likely induce structural disorder in the diluted analogue $\mathbf{2_{1\%}}$. In fact, the powder XRD patterns of $\mathbf{2_{1\%}}$ can mostly be ascribed to the BNAS-11 phase (Fig. S9), as could be expected. This means that while the overall 2D sheet structure remains the same, the packing in the diluted analogue $\mathbf{2_{1\%}}$ may be an intermediate between the two structural phases.

2.2 Magnetic properties

The equilibrium paramagnetic susceptibility χ of the two bulk materials **1** and **2** mostly depict an isolated Cu(II) paramagnetic ion. The χT product for **1** of 0.375 $cm^3mol^{-1}K$ at 100 K agrees well with the expected $S = 1/2$ spin-only value, and a slight decrease is only observed below 10 K, reaching 0.365 $cm^3mol^{-1}K$ at 2 K (Fig. 3 left). This minute decrease can be attributed to very weak antiferromagnetic interactions. A Curie-Weiss analysis of the susceptibility provides a Weiss temperature of –0.064(2) K, confirming that the influence of interactions is weak. The corresponding data for the bulk MOF **2** are almost indistinguishable from those of **1**, with in this case a Weiss temperature of –0.074(2) K (Fig. 3 right). For both materials, field-dependence of the magnetization agrees with the Brillouin function for an $S =$

1/2 paramagnetic ion (insets in Fig. 3), supporting the absence of any strong magnetic interactions.

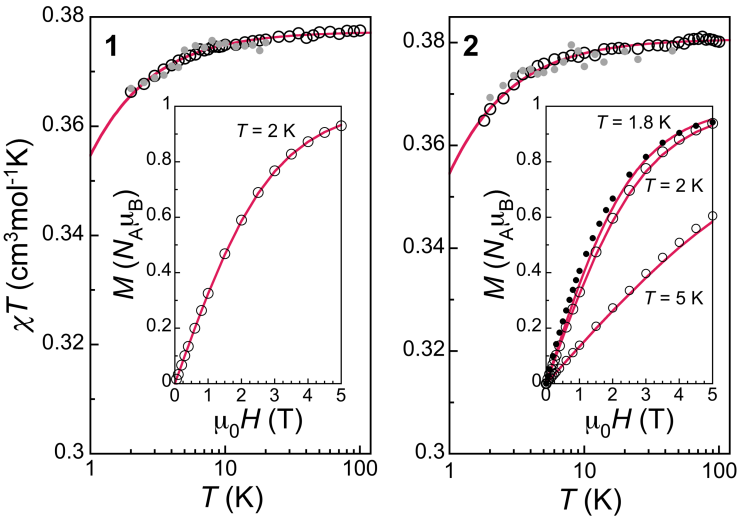

Figure 3: Temperature dependence of χT for **1** (left) and **2** (right) as derived from *dc* measurements at 0.01 T (empty symbols) and zero-field *ac* measurements at 10 Hz (full grey symbols). The solid red lines are Curie-Weiss fits with C = 0.3773(1)/0.3807(2) cm^3mol^{-1} and θ = –0.064(2)/–0.074(2) K respectively. Insets: Magnetization isotherms at the indicated temperatures for both compounds. The magnetization isotherm of a 24-layers [{Cu(TCPP)}Zn_2] nanosheets deposit on Mylar at 1.8 K is also included as full black symbols (right). The solid red lines correspond to the Brillouin function for S = 1/2 and g = 2.0.

The CW X-band EPR spectrum of polycrystalline **1** (Fig S13a) is characteristic of an axial Cu(II) isolated ion showing a clearly resolved hyperfine structure in the parallel feature. No significant modification of the spectrum is observed between 300 and 6 K. The spectra can described by the spin Hamiltonian $H = \mu_B \mathbf{B}\cdot\hat{\mathbf{g}}\,\mathbf{S} + \mathbf{I}\cdot\hat{\mathbf{A}}\cdot\mathbf{S}$ where **S** is the electronic spin (S = ½) and **I** the nuclear spin (I = 3/2) and $\hat{\mathbf{g}}$ and $\hat{\mathbf{A}}$ are, respectively, the gyromagnetic and hyperfine tensor which have axial symmetry. A fairly good description of the spectrum is obtained with principal values $g_{||}$ = 2.2, $g_{\perp}$ = 2.065, $A_{||}$ = 590 MHz and $A_{\perp}$ < 30 MHz (Fig. S13a), in line with those reported for other square-planar Cu(II) porphyrin molecules.[21] Additionally we have measured the CW-EPR of **1sol**, a diluted frozen solution of **1** in MeOH-d^4: EtOH-d^6 1:1 mixture, at 6 K (Fig. S13b). The similarity of the spectra, in particular the position of the features, indicates that the spin Hamiltonian parameters and therefore the electronic structure

of the Cu(II) moiety are similar in solution and in solid **1**. The solution spectrum in addition exhibits a resolved hyperfine structure arising from the coupling with the N nuclei. The X-band CW EPR spectrum of **2** presents differences when compared with that of polycrystalline **1** (Fig. S13b). It does not show any resolved hyperfine structure and presents a strongly anisotropic broadening in such a way that the "parallel" feature is barely detected. This strongly suggests the existence of sufficient exchange interactions between the magnetic moieties to delocalize the spin.[22] This interpretation is reinforced taking into account the spectrum of the magnetically-diluted analogue $\mathbf{2_{1\%}}$ where the spatial correlation length of the inter-moieties exchange interaction should be severely reduced. Indeed, its spectrum (Figure S13b) is similar to that of **1**, with additional resolution of the hyperfine structure due to the coupling with N nuclei, which agrees with the fact the {Cu(TCPP)} unit in **2** is extremely similar to the [Cu(H_4TCPP)] moieties in **1**, and suggests similar spin Hamiltonian parameters as those derived for **1**.

Ac magnetic susceptibility measurements were used to probe the low-temperature dynamics of the magnetization of both bulk materials (Fig. 4 and S10-S12). A non-zero out-of phase susceptibility χ'' is visible only upon application of *dc* magnetic fields, indicative of field induced slow magnetic relaxation. Characteristic relaxation times τ were determined from the frequency-dependence of χ'' at various applied *dc* fields at 1.8 K, reaching various ms at optimal fields. Variable temperature measurements were also performed, at optimal *dc* fields of 0.15 T, 0.3 T and 0.5 T for **1** and 0.1 and 0.5 T for **2**. Within our accessible range of frequency (10 kHz), maxima in χ'' were observed up to 20 K. Similar values of τ were derived by fitting a generalized-Debye model to the data or by simply taking the frequency at which χ'' is maximum and applying the relation $\tau^{-1} = 2\pi\nu_{max}$ (Fig. 4 right). The spin–lattice relaxation of non-interacting paramagnetic centers can act via various acoustic phonon processes usually involving direct one-phonon process, two-phonon Raman processes, or

excitations to energy orbital levels or Orbach process.[23] Interactions, even weak, can also play a dominant role. Here, the spin-lattice relaxation is found to be $\sim H^2$ at low field, which is usually attributed either to lattice two-phonon processes[24,25] or to magnetic interactions.[26] The temperature dependence of the relaxation rate of both compounds is fairly weak and characterized by a dependence $\sim T^n$, with n in the range 1.4-1.7, except at 0.5 T in the case of **2** for which n is even smaller (Fig. 4 right). At temperatures below the material Debye temperature Θ_D, the temperature dependence of the relaxation rate for *isolated* Kramers ions without a real level to be excited, as is the case here, is expected to be of the form $\tau^{-1} = R_{dir}T + R_{Raman}T^9$.[27] However, phonon bottleneck, whose effect is larger at high magnetic concentrations, is known to result in a $\tau^{-1} \sim T^2$. Moreover, the spin-lattice relaxation in **1** at high fields is $\sim H^{-2}$ instead of the $\sim H^{-4}$ field dependence expected for the direct process, dominant at high fields in a Kramers ion. This too is usually ascribed to the effect of phonon bottleneck that slows down the direct relaxation process.[28] Overall, the spin-lattice relaxation in **1** and **2** is likely dominated by two-phonon Raman processes at low fields, and one-phonon direct process at high fields, while being strongly affected by phonon bottleneck. Identifying specific vibrational modes relevant for the spin dynamics could help reduce these effects by adequate synthetic design, but requires combined spectroscopic, calorimetric and theoretical studies, as done recently for the $[Cu(mnt)_2]^{2-}$ ion,[29] that are beyond this work. On the other hand, studies of the spin-lattice relaxation of series of vanadyl complexes have shown that one way to minimize this effect is to increase the stiffness of the molecular qubit environment.[30] Here the porphyrin macrocyle is already quite rigid, so that improvements could only be expected form stiffer 2D frameworks for example using ethynyl-phenyl linkers.

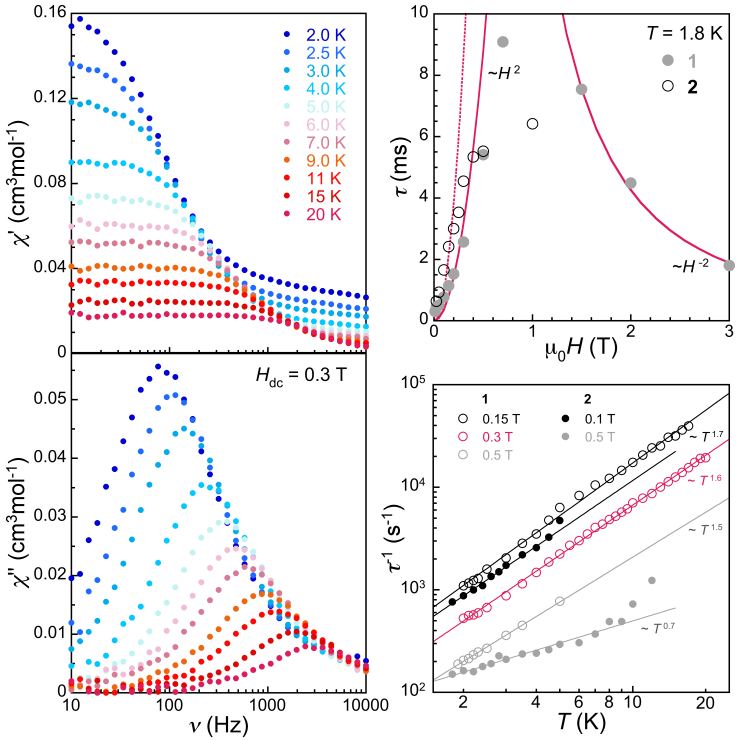

Figure 4. Left: frequency dependence of the in-phase (top) and out-of-phase (bottom) *ac* magnetic susceptibility of **1** at 0.3 T *dc* field. Right, top: relaxation time as a function of the *dc* magnetic field at 1.8 K; solid lines are fits to $\tau \sim H^{2}$ ($\mu_0 H < 1$ T) and $\tau \sim H^{-2}$ ($\mu_0 H > 1$ T). Right, bottom: temperature dependence of the spin-lattice relaxation rate τ^{-1}; solid lines are fits to $\tau^{-1} \sim T^{n}$ (see text).

Interestingly, similar values of τ are observed in both **1** and **2**, indicating the framework structure of the latter does not modify significantly the spin relaxation of the {Cu(TCPP)} unit. In fact, relaxation is slightly slower in the 2D framework material **2**, likely due to a more rigid lattice, *i.e.* a higher Θ_D. More importantly, the fairly long spin-lattice relaxation times, of the order of various ms at low temperatures, suggest that phase coherence times can also be relatively long, as observed for analogous Cu and VO phtalocyanines.[4d,13]

2.3 Evaluation of quantum coherence

To evaluate the quantum coherence of the {Cu(TCPP)} unit, and thus its potential as spin-based qubit, we turn to pulsed EPR spectroscopy. In polycrystalline **1** no electron spin echo (ESE) is observed at temperatures down to 4 K as a likely consequence of the shortening of the relaxation time by spin-spin interactions. To minimize these interactions, diluted samples

are preferred and spin dynamics measurements where done on **1sol**. The CW-EPR measurements (see above and Fig. S13b) suggest that the magnetic moieties keep their structure in solution. The use of deuterated solvents allows reducing the effects of hyperfine interactions with solvent hydrogen nuclei. Using a 2-pulse (2p) sequence, ESE is detected at any magnetic field in the CW-EPR spectrum (Fig. 5). The echo-induced EPR spectrum for **1sol** is indeed in excellent agreement with an absorption analogue of the CW spectrum (Fig. S14), confirming the {Cu(TCPP)} unit presents a measurable quantum coherence.

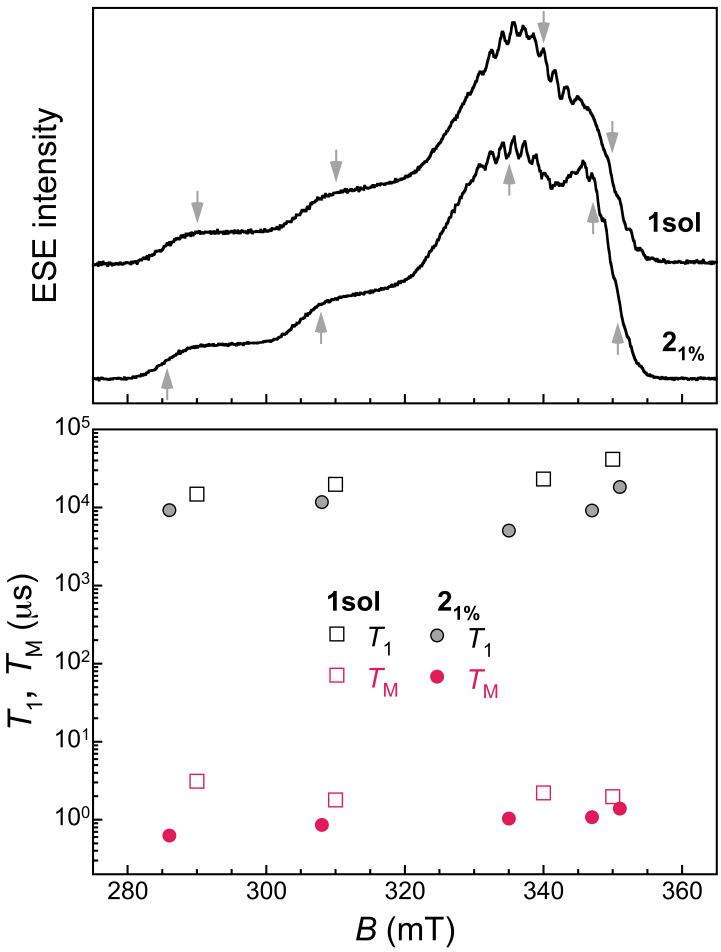

Figure 5. Top: ESE-detected 2p EPR spectrum of the dilute frozen solution **1sol** (ν = 9.7304 GHz, τ = 160 ns) and polycrystalline **2$_{1\%}$** (ν = 9.7581 GHz, τ = 120 ns). The vertical arrows indicate the fields at which spin dynamics have been studied. Bottom: Spin-lattice relaxation (T_1, black symbols) and phase memory times (T_M, red symbols) for **1sol** and **2$_{1\%}$** as indicated.

Phase memory times T_M have been obtained by measuring the ESE following a 2p Hahn sequence of π/2 and π pulses separated by a varying interval τ. The ESE decay was measured

at 6 K at four main features of the spectrum, i.e. 290, 310, 340 and 350 mT (indicated in Fig. 5) The decay is strongly modulated and was reproduced with the function in equation 1

$$y(\tau) = y_0 + A_{2p}e^{-2\tau/T_M}\{1 + ke^{-(2b\tau)^2}\cos(2\pi\nu\tau + \phi)\} \qquad (1)$$

that corresponds to an exponential decay including a modulation due to a Gaussian distribution of frequencies centered on ν (see Fig. S15 and Table S4). The derived values of T_M, in the range 2.4–5 μs, are depicted in Fig. 5 for the different magnetic fields. On the other hand, the mean modulation frequency, ν, increases with the magnetic field, taking values between 1.96 and 2.31 MHz (Table S4), close to twice the nuclear Larmor frequency of ^{14}N (1.08 MHz at 350 mT). Measurements were also conducted at 30 and 60 K at 340 mT (Fig. S16). Interestingly, the phase coherence time appears to be temperature-independent at least up to 30 K where T_M = 2.24(3) μs, similar to the value at 6 K (Fig. 6). At 60 K, T_M has decreased to 0.85(4) μs possibly due to thermal processes associated with spin-lattice relaxation and softening of the glassy frozen solution.[30a,31]

The field and temperature dependence of the longitudinal relaxation time, T_1, was also explored via inversion recovery experiments, in which the ESE signal induced through a Hahn-echo sequence is measured as a function of the delay time, t_d, after an initial inversion pulse (Fig. S17 and S18).[32] In this case an exponential dependence fails to reproduce the observed behavior (as illustrated in Fig. S17a) and we use instead a stretched exponential, that can be given by equation 2 [33,34]

$$y(t_d) = y_\infty - y_0 e^{-(t_d/\beta T_1)^\beta} \qquad (2)$$

that satisfactorily fits the experimental data (Fig. S17b, Table S4). At 6 K, β takes a value close to 0.6 that suggests a distribution of lattice relaxation times whereas the mean value of T_1 increases with the magnetic field, from 14.8 ms at 290 mT to 41.5 ms at 350 mT (Fig. 5). This field dependence is in line with the variation of τ with applied *dc* field derived from *ac* magnetic susceptibility (see above). At 340 mT, T_1 decreases with increasing temperature,

from 23.2(7) ms at 6 K down to 13(1) µs at 60 K (Fig. 6 and Table S5). Although the decrease of T_M observed at 60 K may involve thermally driven relaxation processes, T_1 remains about one order of magnitude higher than T_M, and is therefore not yet the limiting factor for T_M. Overall, the phase memory times for **1sol** are reasonably long, in the range of those found for Cu or VO phtalocyanines.[4d,13] As for these analogues, the present study of the spin dynamics thus demonstrates that the {Cu(TCPP)} unit can be employed to embody a spin qubit with reasonable quantum coherence.

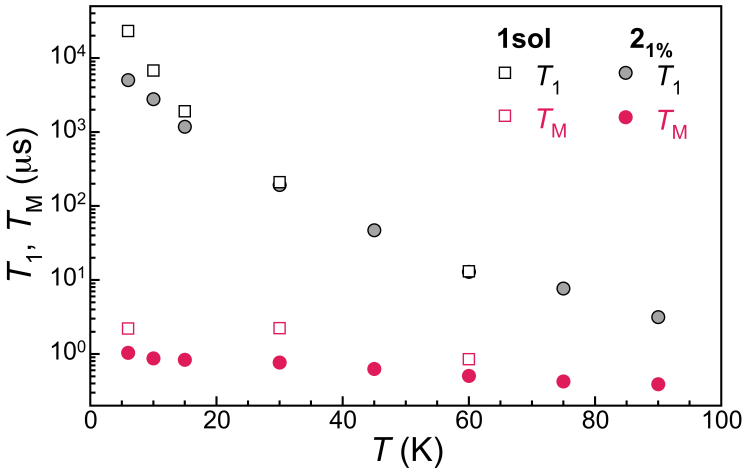

Figure 6. Temperature dependence of the longitudinal relaxation time T_1 and phase memory time T_M for **1sol** and polycrystalline **2$_{1\%}$** as indicated and at respectively B = 340 and 335 mT.

No ESE has been detected in polycrystalline **2**, down to 6 K. Similarly to **1**, this is likely due to the spin-spin interaction present in such magnetically concentrated samples. Nevertheless, a 2p ESE is detected in the case of the dilute analogue **2$_{1\%}$** for any magnetic field in its CW-EPR spectrum. The 2p ei-EPR spectrum of polycrystalline **2$_{1\%}$** is given in Fig. 5 and compared with its CW-EPR analogue in Fig. S14, showing that both, ei- and CW-EPR spectra, arise from the same magnetic entity. This ESE observation allows performing similar experiments and data analysis as those described above for **1sol**, thus determining the field and temperature dependence of both, the phase memory time, T_M, and the mean longitudinal relaxation time, T_1, of **2$_{1\%}$** (Fig. S19-S22, Tables S6 and S7). The dependence of T_M and T_1

with the magnetic field at 6 K is depicted in Fig. 5, while their temperature variations are included in Fig. 6. As for **1sol**, an exponential function fails to describe the inversion recovery behavior observed in $\mathbf{2_{1\%}}$ and a stretched exponential dependence was used to describe it. Therefore, T_1 values have to be read as the mean value of a distribution of longitudinal relaxation times. At 6 K, values of T_1 in the range 9.3-18.5 ms are found for $\mathbf{2_{1\%}}$, lower but of the same order as those of **1sol**. In fact, the temperature dependence of T_1 derived for $\mathbf{2_{1\%}}$ is almost identical to that of the frozen solution (Fig. 6), indicating the solid-state 100-fold dilution is sufficient to suppress the effect of spin-spin interactions. Indeed, the phase memory time, T_M, at 6 K in the diluted $\mathbf{2_{1\%}}$ is of the same order as found in frozen solution. At 335 mT, T_M of $\mathbf{2_{1\%}}$ decreases only very slightly with increasing temperature from 1.04 μs at 6 K to 0.39 μs at 90 K (Fig. 6 and Table S7). Overall, the {Cu(TCPP)} unit in $\mathbf{2_{1\%}}$ maintains coherence times about twice smaller than **1sol** over the whole studied temperature range. To explain the slightly shorter T_M in $\mathbf{2_{1\%}}$, other aspects than a possibly insufficient dilution may be relevant. In this respect, it should be mentioned that the strong modulation of the ESE decay present in **1sol** is not observed in $\mathbf{2_{1\%}}$. In fact, only a very weak modulation is present (see *k* values in Tables S4 and S6 respectively for **1sol** and $\mathbf{2_{1\%}}$), with a frequency of *ca.* 12-15 MHz, therefore corresponding to coupling with protons. It is important to realize that the former results do not guarantee the absence of a modulation due to interaction with protons in the 2p-ESE decay of **1sol**. Indeed, it could be present but buried by the heavy modulation due to interaction with the ^{14}N nuclei, which is absent or significantly reduced in the case of $\mathbf{2_{1\%}}$. The observed heavy modulation strongly suggests that the ^{14}N coupling is close to the "exact cancellation" condition[35] in **1sol**. Consequently, one of the nuclear transitions in an electronic manifold is practically isotropic, so that it is enhanced in orientationnaly disordered systems. Departure from this "exact cancellation" condition due to a slight modification of the effective hyperfine coupling result in a significant decrease of the modulation depth and consequently the ^{14}N contribution becomes undetectable.[35b] The displacement of the Cu(II) ions slightly off

the porphyrin N_4 plane in $\mathbf{2}_{1\%}$ due to some structural disorder induced by the dilution in a different structural phase would very likely involve modification of the effective hyperfine coupling, which even modest would result in departure of the "exact cancellation" condition, and therefore explain the absence of strong modulation of the ESE decay in $\mathbf{2}_{1\%}$. In any case, the quantum coherence of the {Cu(TCPP)} node in its diluted 2D MOF $\mathbf{2}_{1\%}$ remains reasonably long, even at such relatively high temperatures as 90 K. This therefore validates the strategy envisioned here, for which these robust structurally rigid qubit frameworks now need to be made as on-surface nanosheets.

2.4 Fabrication and characterization of 2D MOF nanosheets

{Cu(TCPP)} building blocks were assembled into a 2D framework layer at the air/water interface, following the procedure used by Makiura for {Co(TCPP)}[17] and adjusting conditions to ensure that similar highly crystalline MOF layers are obtained. Thus, a $CHCl_3$:MeOH solution of **1** was spread over a $ZnCl_2$ aqueous solution in a Langmuir trough, and the surface pressure-area (π-A) isotherms were recorded. These were found to be similar to that reported for the {Co(TCPP)} / Cu system (Fig. S24), albeit only for Zn(II) concentrations of the subphase equal or superior to 0.1 M, while no differences were observed with the Cu(II) subphase from 0.0001 to 0.1 M.[17b] For lower Zn(II) concentrations of the subphase, the Langmuir isotherm has the same shape but shifts towards lower areas. The larger molecular areas compared with those observed when using pure water as subphase are still consistent with the binding of Zn(II) ions to the metalloporphyrin. Moreover, the similarity of the π-A isotherm and molecular areas obtained with more concentrated subphases compared to those reported previously for the Cu(II) subphase indicate that a similar molecular arrangement occurs. The only difference is that a higher subphase concentration is required using $ZnCl_2$. This concentration dependence is likely associated with a less efficient formation of 2D domains with Zn(II) ions than with the more labile Cu(II)

ions. Overall, and by analogy with the {Co(TCPP)} / Cu system, domains of a crystalline 2D framework are likely formed. To confirm this, in situ synchrotron grazing-incidence X-ray diffraction measurements were performed under the same conditions as those used for the transfer to substrates (see below and experimental section). The in-plane XRD pattern shows two clear diffraction peaks at 2θ = 5.2 and 7.1º (1.701 and 1.252 nm) that are fully consistent with the (010) and (001) reflections of bulk **2**, albeit with a slightly expanded cell with b = 17.00 Å and c = 12.95 Å (Fig. 7 left). The absence of diffraction in the expected range for the corresponding (011) reflection likely indicates a higher pseudo-tetragonal symmetry of the nano-sheets with respect to bulk **2**. The highly crystalline nano-sheets were compressed and transferred at 5 mNm^{-1} onto various types of substrates for their characterization, either as mono- (i.e. 1 transfer) or multiple layers. Specifically Si(100) was used for AFM and XPS, quartz for absorption spectroscopy, Mylar for magnetic measurements, absorption spectroscopy, AFM and XPS, and carbon-coated Cu grids for TEM.

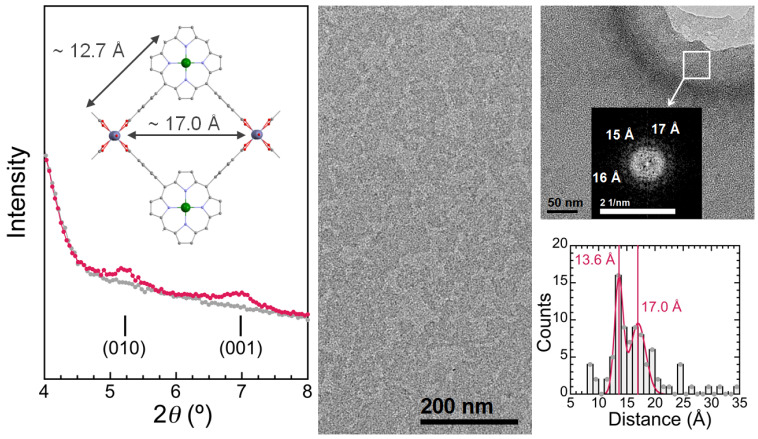

Figure 7. Left: in-situ synchrotron GIXS of [Cu(H_4TCPP)] over a 100 mM $ZnCl_2$ subphase at a surface pressure of 5 mNm^{-1} (red symbols). Background of the sole subphase is shown as grey symbols. Vertical ticks indicate the (010) and (001) reflections of compound **2** with a slightly expanded cell, as shown as inset. Middle: characteristic TEM image of 1-cycle transfer. Right, top: example of FFT of a selected TEM image area, in which reciprocal space points can be observed and assigned to characteristic distances. Right, bottom: histogram collecting characteristic distances of several selected areas, together with a bimodal normal distribution fit of the data, performed avoiding artifacts arising from the carbon coating (see SI).

TEM images of the material transferred at 5 mNm^{-1} directly onto the carbon-coated Cu grid depict a rather homogeneous and continuous deposit (Fig. 7 and S25), in which domains can be distinguished. FFTs of many areas point at the presence of characteristic intermetallic distances of *ca.* 1.70(2) and 1.36(1) nm (Fig. 7), in good agreement with the in-situ GIXS data, and thus indicating crystalline domains of the 2D framework are successfully transferred. In agreement with the formation of [{Cu(TCPP)}Zn_2] sheets, absorption spectra after successive deposition cycles (Fig. 8 and S4) show a characteristic spectra similar to that of [Cu(H_4TCPP)], with Soret and Q-bands respectively at 416.0, 552.5 and *ca.* 593 nm. The red-shift of the Q-bands with respect to **1** can result from the deprotonation and coordination of the carboxylic acid groups as well as from orientation effects associated with the 2D structure and deposition. The identical spectra obtained at various positions of the substrate also indicate macroscopically homogeneous deposits. The magnitude of the maximum absorbance of the Soret band after one sole transfer is slightly inferior but very close to that calculated for one [{Cu(TCPP)}Zn_2] sheet,[36,37] pointing at a good and almost complete coverage of the surface with nano-sheets, considering the transferred material is made of domains. This is in good agreement with AFM observations (see below). The observed near-linear increase with the number of transfer cycles indicates that this is maintained throughout multiple transfers. The slight departure from the linear increase after 16 cycles may be ascribed to the small increase of the surface roughness making the transfer less efficient.

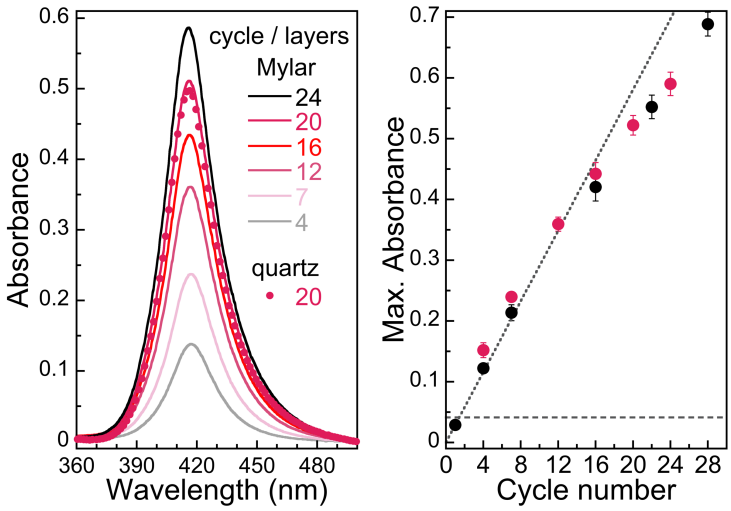

Figure 8. Left: evolution of the absorption spectra of successive steps of the formation of a 24-layers [{Cu(TCPP)}Zn_2] deposit on Mylar. The spectrum corresponding to a similar 20-layers deposit over quartz (dot symbols) is also included to show the reproducibility of the process over different substrates. Right: maximum absorbance of the Soret band as a function of the number of deposition cycle, for two separate experiments, showing again a good reproducibility. Error bars represent the standard deviation from the measurement of the spectra taken over three points of the substrate. The horizontal dashed line represents the absorption calculated for a monolayer.[36,37] The dotted line corresponds to the expected increase per layer considering the absorption for 1 layer.

Atomic force microscopy (AFM) images indicate that a single transfer results in a full and homogeneous coverage of the substrate (Fig. 9A), in agreement with TEM observations. Such a uniform coverage is maintained upon multiple deposition cycles, as observed for a 28-layers deposit (Fig. 9B), and in line with the linear increase of the maximum absorbance of the Soret band with the number of transfer cycles. The deposits are structured by nanosheet rounded domains, a morphology similar to that observed for the {Co(TCPP)} / Cu analogue deposits.[17b] In particular, the lateral size of the domains, *ca.* 50-100 nm, is in the range previously deduced by in-situ synchrotron GIXS for the {Co(TCPP)} / Cu nanosheets formed interfacially, as well as with those observed in TEM images. The roughness does not significantly increase with the number of layers, with a RMS of 0.52 nm for a single cycle and 2.43 nm for a 28-cycle transfer. The estimated height of the domains is rather homogeneous, in the range 1–3 nm. The average height of 1-cycle transfer, 2.1 nm (Fig. 9A right) would correspond to few –1 to 4– stacked layers, considering an interplane separation of 0.7 nm,

slightly larger than in the structure of **2**. Considering the dense surface coverage and the necessary defects due to the packing of domains, this agrees with the magnitude of the maximum absorption at the Soret band, which is close to that calculated for 1 continuous molecular layer perfectly parallel to the surface. Adequate compression of the pre-assembled domains is key to yield the obtained dense full substrate coverage. Indeed, transfer conducted at 0.5 mNm^{-1} only provides an uneven partial coverage (Fig. S26), while higher surface pressures (above 30 mNm^{-1} for metalloporphyrin analogues[18-20]) result in increased surface roughness due to deformation or stacking of neighboring sheets.

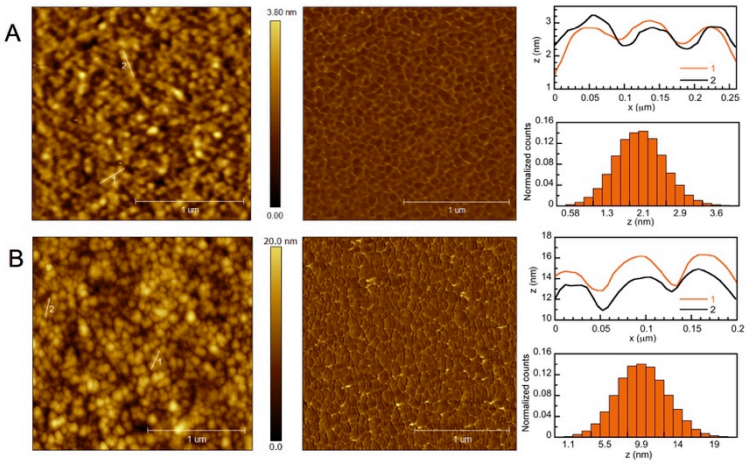

Figure 9. AFM observations for 1-cycle (A) and 28-cycle (B) [{Cu(TCPP)}Zn_2] deposits on Mylar. Left: topography images with rms roughness of 0.52 nm (A) and 2.43 nm (B). Middle: phase images shows full surface coverage. Right: Section profiles and height histograms showing the films are nanostructured by small domains of about 50-100 nm size.

X-ray photoelectron spectroscopy (XPS) confirms the presence of Cu and Zn (Fig. S28) with peaks at binding energies in agreement with those of the expected bonding states, as well as the absence of Cl thereby precluding that $ZnCl_2$ is deposited. High-resolution spectra for the Cu 2p region show that the shape of the peaks and the BE values of the multilayers are very close to those of **1**. The Zn/Cu ratio of 2.06 derived from high-resolution spectra is consistent with the value expected for 2D square grid layers as in **2**.

The CW-EPR spectrum of a 24-layers [{Cu(TCPP)}Zn_2] nanosheets deposit on Mylar depends on the magnetic field angle with respect to the normal to the substrate, ϕ. While the

spectrum observed when the magnetic field lays in the sheet plane ($\phi = 90^{o}$) consists of a simple line in the "perpendicular" feature of the spectrum of **1**, the spectrum taken with the magnetic field normal to the sheet ($\phi = 0^{o}$) is dominated by the parallel features showing a clear hyperfine structure with the Cu nuclei (see Figure 10 and Figure S23 for the full rotation). Due to the low signal to noise ratio likely resulting from the low amount of magnetic entities, an in-depth study of the spectrum and its dependence on ϕ cannot be done. However, the observed dependence of the CW-EPR spectrum with ϕ clearly indicates that the Cu(II) moieties are mainly disposed with their CuN_4 plane parallel to the substrate, confirming an homogeneous orientation of the {Cu(TCPP)} moieties. This validates the advantage of the 2D framework strategy that enforces a common orientation of the qubit nodes. In spite of that, the observation of a minor "perpendicular" contribution in the $\phi = 0^{o}$ spectrum does indicate either some structural defect within the nanosheets, and/or, more likely, a distribution of nanosheets orientation, probably due to the multilayer nature of the studied deposit. Similarly to **1** and **2**, the magnetization *vs.* field curve of the same 24-layers deposit on Mylar agrees with a Brillouin function (Fig. 3 right), only with a scale factor corresponding to approximately 9.54×10^{15} spins per cm^2. Considering a surface density of one Cu(II) ion per 2.89 nm^2 as derived from the in-situ GIXS data, this translates into an equivalent of 80 molecular planes, i.e. each transfer cycle would result in the deposition of 3.3 molecular planes. Within the assumptions made and experimental errors, this is consistent with the corresponding estimations made through AFM and absorption spectroscopy.

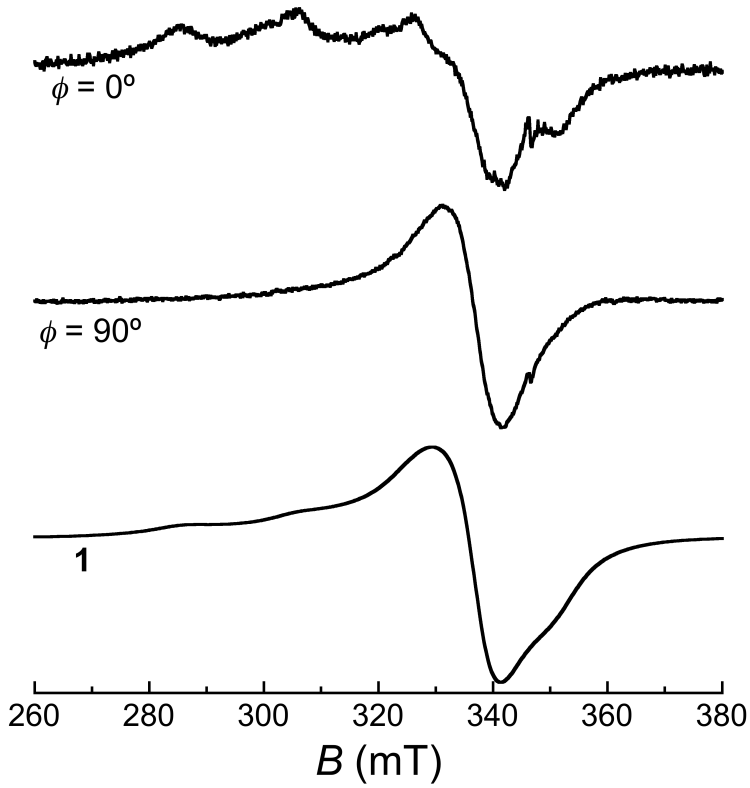

Figure 10. CW-EPR spectra of a 24-layers [{Cu(TCPP)}Zn_2] nanosheets deposit on Mylar at 6 K with magnetic field parallel (ϕ = 90º) and perpendicular (ϕ = 0º) to the substrate. The CW-EPR spectrum of **1** is shown for comparison (bottom trace).

These results altogether provide confident proof that crystalline 2D MOF nanosheets of {Cu(TCPP)} units connected through diamagnetic $Zn_2(COO)_4$ paddle-wheel nodes, similar to those found in **2**, are successfully constructed and transferred onto different substrates, either as mono- or multiple layers. Although no ESE could be detected for the 24-layers [{Cu(TCPP)}Zn_2] nanosheets deposit, this is a likely consequence of significant shortening of T_M due to spin-spin interactions, as in polycrystalline **2**. In analogy with the polycrystalline samples, it is reasonable to consider that a magnetically-diluted deposit would present similar quantum coherence as $\mathbf{2}_{1\%}$, although much thicker deposit would be necessary to reach the detection limit of our pulsed-EPR instrument.

2.5 Towards integration into hybrid devices: dilution and on-surface structuration

Reading and manipulation of qubits state towards quantum computation will necessarily require their integration into solid-state devices, and therefore their structuration on surfaces. This is the case for our recent proposal of a hybrid quantum processor, whose feasibility relies on the possibility of integrating a molecular qubit with sufficiently long coherence time within a nano-constriction of about 100 nm width.[8,38] As we have shown so far, the approach based on 2D MOF with qubit node evaluated here allows to maintain reasonable coherence time while also ensuring a reproducible and homogeneous qubit orientation and environment. Interestingly, the 50-100 nm lateral size of the nanocrystalline domains deposited appear nicely suited for the required spacing in the device. A key remaining requirement for an adequate integration are that only one qubit be coupled per constriction, which translates into the necessity to control the location of isolated 2D nanosheet domains as well as to be able to dilute these with non-magnetic nodes. This section provides evidence that both aspects are feasible.

To demonstrate that deposits of 2D diluted frameworks can be elaborated, a solution containing both **1** and the free-base H_6TCPP in a 1:4.4 molar ratio was used to prepare a 20-layers deposit following the same Langmuir-Schaefer method as for the pure [{Cu(TCPP)}Zn_2] deposits. Because the free-base H_6TCPP does not metallate under these conditions, the composition of the deposit is *a priori* [{Cu(TCPP)}$_{0.23}$(H_2TCPP)$_{0.77}Zn_2$]. In terms of magnetic dilution this is a similar outcome as a hypothetical $\mathbf{2_{23\%}}$ solid. The UV-Vis absorption spectrum of the resulting deposit reveals the absorption bands visible in each of the MOF multilayer constituents (Fig. 11), in a similar manner as the admixture solution shows the characteristic Q-bands of each of its components (Fig. S5). XPS survey spectrum confirms the presence of Cu and Zn in the [{Cu(TCPP)}$_{0.23}$(H_2TCPP)$_{0.77}Zn_2$] deposit. Compared to those obtained on the pure [{Cu(TCPP)}Zn_2] deposit, the high resolution spectra of the Cu 2p and Zn 2p regions displays a smaller Cu contribution in agreement with the qubit porphyrin dilution (Fig. 11). The shape of the peaks in the Cu 2p region and their binding energies are

similar but weaker, satellite structures being only weakly visible. In contrast, peaks of the Zn 2p region are clearly visible and similar. Overall, the nanosheets [{Cu(TCPP)}Zn_2] deposits can be magnetically diluted in a similar manner as **2**, albeit with un-metallated {H_2TCPP} nodes instead of {Zn(TCPP)}.

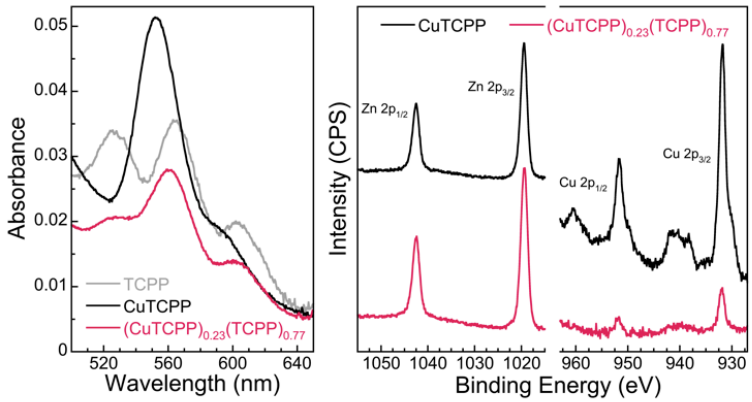

Figure 11. Left: UV-vis absorption spectra of 20-layers deposits of [(H_2TCPP)Zn_2] (grey), [{Cu(TCPP)}Zn_2] (black) and [{Cu(TCPP)}$_{0.23}$(H_2TCPP)$_{0.77}Zn_2$] (red) on quartz substrates. Right: high resolution XPS spectra of the Zn 2p (full scale is 6000 CPS) and Cu 2p (full scale is 43000 CPS) regions from 20-layers deposits of [{Cu(TCPP)}Zn_2] (black) and [{Cu(TCPP)}$_{0.23}$(H_2TCPP)$_{0.77}Zn_2$] (red).

To demonstrate isolated nano-domains of the 2D qubit framework can be integrated at specific positions of a device, their direct formation onto the substrate surface was pursued. Besides the necessary positioning, this approach should ensure stronger coupling to the resonator. As mentioned here and demonstrated previously,[18] the MOF crystalline nanosheets are built at the air/liquid interface by self-assembly upon reaction of the [Cu(TCPP)] metalloporhyrin building unit and the Zn(II) ions in the aqueous subphase. Interestingly, these nano-assemblies also form when following procedures of alternate immersions of a substrate in adequate solutions,[39] suggesting the 2D nanosheet formation is inherent to this MOF coordinative reaction. We therefore devised a protocol aimed at local on-surface 2D MOF formation, taking advantage of the fact the nanosheet formation is expected to proceed instantaneously.[18] Mica was used as substrate to better mimic the native oxide layer surface of the devices.[8] First, a 100 µL droplet of 0.1 M $ZnCl_2$ aqueous solution was dropped on mica,

which spreads covering the surface thanks to the hydrophilic character of the substrate. Five 0.5 μL droplets of a [Cu(H_4TCPP)] $CHCl_3$:MeOH solution are then immediately delivered atop. The water is then let to evaporate completely. The strategy is based on the highly volatile character and non-miscibility with water of the [Cu(H_4TCPP)] solution. The procedure is repeated four times to allow an easier detection of the nanodomains by the AFM. Finally, the mica is submerged for five minutes in Milli-Q water to remove unreacted or physisorbed components. AFM observations are shown in Fig. 12.

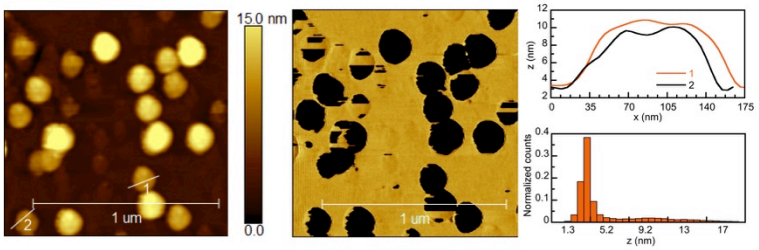

Figure 12. Characteristic AFM observations after local in-situ formation of [{Cu(TCPP)}Zn_2] nanosheets. Topography (left) and phase (middle) show domains similar to those formed through the Langmuir-Schaefer protocol. Right: section profiles and height histogram showing domains size about 50-100 nm and heights up to 3.3 nm.

Nanosheet domains similar to those fabricated by the Langmuir-Schaefer protocol are visible, with lateral sizes within the expected 50-100 nm range and heights of *ca.* 3.3 nm. Very few higher domains with heights up to 15 nm are also observed, but likely due to an un-optimized washing procedure.[39] When omitting the addition of the [Cu(H_4TCPP)] solution no domain at all are formed (Fig. S27), corroborating the domain formation emerges from the in-situ coordination of the metalloporphyrin units and the Zn(II) ions. The flat nature and very limited thickness of the observed domains also point at an overall homogeneous and controlled orientation of the 2D nanosheets parallel to the substrate. Clearly, this protocol demonstrates that isolated nanosheet domains of [{Cu(TCPP)}Zn_2] can be formed directly on a solid substrate. Interestingly, the nanosheet domain sizes are similar to the 100 nm constrictions currently considered for realizing our proposed hybrid quantum architecture. This means that one nanosheet per constriction would suffice, provided it contains only one

qubit node. Considering the average lateral size of the observed nanosheet domains and the density of [CuTCPP] nodes derived from the structure, the dilution necessary to have only one [CuTCPP] qubit node per nanosheet domain can be estimated to be of the order of 0.1%, which seems feasible. All this represents a key preamble to enable their integration at controlled localization of devices, which will require optimization of the conditions used here in combination with local deposition techniques.

3. Conclusion

The foregoing experiments and results demonstrate that a Cu(II) metalloporphyrin molecule, with significant quantum coherence in dilute frozen solution making it a potential spin-base qubit, can be assembled into 2D grids through diamagnetic Zn(II) nodes, both as a bulk material and as nanosheets deposited on a variety of substrates. The solid-state spin-lattice relaxation of the isolated qubit and its 2D assembly are shown to be similar, indicating the assembly does not significantly modify the qubit environment. This is confirmed by the estimation of phase-memory times in magnetically-diluted 2D MOF of the same order as in frozen solution. Preliminary studies also show that magnetically diluted 2D framework nanosheets can also be made, using the metal-free porphyrin. A proof-of-concept that the 2D nanosheets can be formed directly in-situ at specific locations of a substrate is also provided. Both these aspects are key to integrate the Cu(II) metalloporphyrin qubit at constrictions along superconducting coplanar resonators so as to build an hybrid quantum architecture.[7] To reach the required accurate positioning of the nanosheet, our preliminary protocol will now have to be reproduced using scanning probe lithography techniques, thus depositing extremely small quantity of materials. Although challenging, this appears feasible since these techniques have been able to deposit a controlled number of isolated magnetic molecules on the most sensitive areas of other solid-state devices such as μ-SQUID[40] or μ-Hall[41] sensors. An alternative procedure for the formation of the nanosheets locally at the nanoconstriction

would be the use of dip-pen nanolithography with microfluidic pens, allowing femtolitre chemistry on surfaces by handling and mixing femtolitre volumes of reagents.[42] One critical issue could be the ability to reliably control the degree of magnetic dilution at the single nanosheet level, to ensure only one qubit is present at each constriction of the proposed hybrid arquitecture. Devices have increased their sensitivity by miniaturization to maximize the coupling between the device and the sample. Our approach now opens the possibility of integrating one sole spin qubit at specific locations of what would be a prototype of spin-based quantum processor. The same approach could probably be applied to clock-like qubits since clock transitions with relatively large quantum coherence have recently been evidenced in a related [Co(TCPP)] 3D framework.[43] We currently explore strategies aiming at improving the coherence times using vanadyl analogues to the [CuTCPP] qubit node, as well as devising nodes with nuclear-spin free ligands allowing to build other kinds of 2D networks.

4. Experimental Section

Materials:

5,10,15,20-tetrakis(4-carboxyphenyl)porphine (H_6TCPP, >97%) was purchased from TCI. Cu(acetate)$_2$·H_2O (>99.0%), $ZnCl_2$ (>98%), $Zn(NO_3)_2$·$6H_2O$ (98%) and Reagent/HPCL grade solvents N,N'-dimethylformamide (DMF), chloroform and methanol were purchased from Aldrich and used without further purification.

Synthesis of 2[Cu(H_4TCPP)]·4.5DMF·1.5H_2O (**1**). H_6TCPP (253 mg, 0.31 mmol) was dissolved in 200 mL DMF previously warmed to 120ºC. After 5 min stirring, a slight excess of Cu(acetate)$_2$·H_2O (64 mg, 0.317 mmol) was added and the mixture stirred under reflux for 90 min. After cooling in an ice/water bath, 200 mL H_2O were poured into the reaction mixture under vigorous stirring. After removing by filtration a small amount of violet solid (17 mg), the reaction mixture was kept unperturbed at 4ºC. Thin shiny plate crystals of **1** formed upon standing and were recovered by filtration after 15 days. A second crop of crystals was

obtained upon letting the filtrate stand at 4ºC. The total yield of crystals of **1** was 190 mg (59% based on TCPP, 0.18 mmol). Anal. calcd. for $C_{48}H_{28}CuN_4O_8 \cdot 2.25DMF \cdot 0.75H_2O$ (found): C, 63.83 (63.4); H, 4.43 (4.3); N, 8.50 (8.7) weight %. m/z (MALDI-TOF-MS in $MeOH/CHCl_3$, matrix: ditranol): 851.2.

Synthesis of [{CuTCPP}$Zn_2(H_2O)_2$]·2DMF (**2**). 1 (19.0 mg, 0.018 mmol Cu), $Zn(NO_3)_2 \cdot 3H_2O$ (23.8 mg, 0.08 mmol) and 10 mL DMF were put into a 23 mL Teflon-lined PARR acid digestion bomb. The bomb was warmed in an oven to 120ºC, kept at this temperature for 48 h and cooled down slowly to room temperature. Tiny purple crystals were recovered by filtration, washed with little DMF, little acetone and dried in air, except a portion kept in DMF and from which crystals were taken for single-crystal X-ray diffraction. The total yield of crystals of **2** was 19.0 mg (90% based on [$Cu(H_4TCPP)$]). Anal. calcd. for $C_{54}H_{42}CuN_6O_{12}Zn_2$ (found): C, 55.85 (55.4); H, 3.65 (3.6); N, 7.24 (7.1) weight %. The same synthetic conditions were used to form a 100-fold magnetically diluted analogue $\mathbf{2_{1\%}}$ using a mixture of 1 and H_6TCPP in appropriate amounts. Because the H_6TCPP coordinates Zn(II) ions under these conditions,[15c] an adequate excess zinc nitrate was added and the formulation of the resulting framework is $[\{CuTCPP\}_{0.01}\{Zn(H_2O)TCPP\}_{0.99}Zn_2(H_2O)_2]_\infty$. The relative Cu:Zn metal content was confirmed by ICP-AES to be close to the expected value at 0.003.

Langmuir and Langmuir−Schaefer Film Fabrication.

Surface pressure−area (π−A) isotherms were obtained using a Teflon Langmuir trough NIMA model 702 (dimensions 720 mm x 100 mm). Langmuir-Schaefer films were made with a KSV-NIMA trough model KN 2003, with dimensions of 580 mm × 145 mm. In both cases, compression was performed by a symmetric double-barrier system at constant speed of 7.5 $cm^2 \cdot min^{-1}$. These troughs were kept in a clean room inside closed cabinets and the temperature was maintained at 293 K (±1 K). Ultra-pure Milli-Q water (ρ = 18.2 MΩ·cm) was employed to prepare the $ZnCl_2$ solutions used as subphase. Different $ZnCl_2$ subphase concentrations were tested with H_6TCPP until surface pressure−area (π−A) isotherms

provided a molecular area in agreement with those reported for the H_6TCPP/$CuCl_2$ system,[17] which was obtained using a 0.1 M $ZnCl_2$ concentration. Films were subsequently prepared using this subphase concentration. Solutions of **1** (0.1 mM) and H_6TCPP (0.11 mM) were prepared by dissolving respectively 2.07 mg and 2.05 mg in 25 mL of a chloroform/methanol mixture (3:1, v/v). Admixture **1**:H_6TCPP solution was prepared by mixing the components in volume proportions of 1:4, corresponding to concentrations of 0.02 and 0.088 mM for **1** and H_6TCPP, respectively. In a Langmuir-Schaefer experiment procedure, the through was carefully cleaned with acetone and chloroform, and ultimately filled with Ultra-Pure Milli-Q water, removed by vacuuming, before filling it with 0.1 M $ZnCl_2$ solution. The subphase was then carefully cleaned by closing the barriers down to 40 mm distance and mild surface-touch vacuuming intra-barriers area. After opening the barriers to the maximum area, the system was let to equilibrium for 5 minutes. The porphyrin solution was carefully spread drop-by-drop onto the subphase using a Hamilton microsyringe held very close to the subphase surface, and left to evaporate for 20 minutes before starting the compression. Substrates (quartz, Mylar, Si wafer) were cleaned by 15 min ultrasonication, successively in chloroform, acetone and ethanol. Transfers were carried out by horizontal-dipping at a surface pressure of 5 $mN \cdot m^{-1}$, the substrate being approached to the surface at 0.2 $mm \cdot min^{-1}$ and raised at 10 $mm \cdot min^{-1}$. Between successive transfers, the substrates were cleaned by gently flushing with Milli-Q water, submerging in Milli-Q water for 3 min, and drying under a N_2 flush, to remove unreacted or physisorbed components.

X-ray Crystallography:

The available crystals were extremely thin plates making the use of synchrotron radiation necessary. Crystals of **2** were particularly small and thin, and all crystals tested were either not single (several plates stacked) or twinned. Diffraction was systematically poor to very poor, probably a combined effect of the small size, twinning and diffuse solvent area. Data for **1** and **2** were collected at 100 K on Beamline 11.3.1 at the Advanced Light Source (Berkeley,

USA), on a Bruker D8 diffractometer equipped with a PHOTON 100 CCD detector and using silicon (111) monochromated synchrotron radiation (λ = 0.7749 Å), on purple plates respectively of dimensions 0.13x0.08x0.01 mm^3 and 0.05x0.05x0.01 mm^3. The crystals were mounted with little Paraton N grease on a MiTegen kapton loop and placed in the N_2 stream of an Oxford Cryosystems Cryostream Plus. For **1**, data reduction and absorption corrections were performed with SAINT and SADABS.[44] For **2**, twinning was detected using RLATT[44] and then analyzed with CELL_NOW[45] that found the proper unit cell, twinning law and ascribed reflections to either or both components. Cell refinement and integration were then performed by SAINT as a 2-component twin, keeping the cell of both components identical. TWINABS[45] was used for absorption corrections and produced HKLF4 and HKLF5 data, respectively for initial structure solution and final refinement. Structures were solved with SHELXT[46] and refined on F^2 with SHELXL-2014.[47] All details can be found in the supplementary information in CIF format as well as in CCDC 1555581 (**2**) and 1555582 (**1**) that contain the supplementary crystallographic data for this paper. These data can be obtained free of charge from The Cambridge Crystallographic Data Centre.

Physical characterization:

Infra-red spectra were acquired on neat samples using a Perkin Elmer Spectrum 100 apparatus equipped with an ATR device.

UV−vis spectra were acquired with a Varian Cary 50 spectrophotometer. For deposits, the substrates were placed so that the film plane was normal to the incident light beam, and spectra were systematically acquired at 3 positions of the substrate.

Synchrotron Grazing-Incidence X-ray Scattering (GIXS) was carried out at Sirius beamline[48] of the SOLEIL synchrotron (Paris, France). The energy of the incident X-ray was 8 keV (λ = 0.155 nm) and the beam size was 0.1 × 2 or 0.5 mm^2 (V×H). The incidence angle was 1.32 mrad, below the critical angle of the air-water interface (2.1 mrad at 8 keV).

Transmission electron microscopy (TEM) was used to study the interatomic distances of the 2D network of [{Cu(TCPP)}Zn_2] deposits. For this purpose, the nanosheets formed at the air-water interface were transferred at 5 mNm^{-1} directly onto TEM carbon-coated Cu grid, in particular, Carbon Type-B 400 mesh from TED PELLA, INC. The grid was previously placed almost entirely floating over a glass slide, only attached to it by two tiny double-sided bonding tape pieces of the width of the grid border. Observations were done at the Electron Microscopy unit of the Servicio General de Apoyo a la Investigación-SAI, Universidad de Zaragoza with a JEOL 2000 FXII instrument working at an acceleration voltage of 200 kV. Fast Fourier Transforms (FFTs) of the acquired images were analyzed to find interatomic distances.

X-ray Photoelectron Spectroscopy (XPS) measurements were performed in a Kratos AXIS SUPRA spectrometer, using a monochromatized Al Kα source (1486.6 eV) at the Laboratorio de Microscopías Avanzadas (LMA). Wide scans were acquired at analyzer pass energy of 160 eV, whereas high-resolution narrow scans were performed at constant pass energy of 20 eV. The spectra were obtained at room temperature. The binding energy (BE) scale was internally referenced to the C 1s peak (BE for CC=284.9 eV).

Magnetic measurements were performed with a commercial magnetometer equipped with a SQUID sensor and a commercial Physical Properties Measurement System (PPMS), both hosted by the Physical Measurements Unit of the Servicio General de Apoyo a la Investigación-SAI, Universidad de Zaragoza. The diamagnetic contributions to the susceptibility were corrected using Pascal's constant tables. Direct current (dc) data were collected between 2 and 300 K with an applied field of 100 Oe. Alternating current (ac) data were collected with an applied field of 4 Oe oscillating at different frequencies in the range $0.1 \leq \nu \leq 10\,000$ Hz.

Electron Paramagnetic Resonance (EPR) experiments, both continuous wave (CW) and pulsed time domain (TD), were performed with a Bruker Biospin ELEXSYS E-580

spectrometer operating in the X-band, using a gas-flow Helium cryostat for low-temperature experiments. TD-EPR studies were done on a frozen solution **1sol** (0.46 mmol/L 1 in 1:1 mixture of fully-deuterated methanol and ethanol) and on $\mathbf{2_{1\%}}$. 2p and Inversion Recovery ESE-detected as well as preliminary nutation experiments were performed. In these experiments the length of the $\pi/2$ pulse was, typically, 16 ns whereas the length of the π pulse was 24 ns. In the preliminary nutation experiments, only few cycles were observed and the decay time of the nutation signal was significantly shorter than T_M, due to the effect a distribution of frequencies. First, the spatial disorder due to the frozen solution or polycrystalline character of the sample implies a distribution of frequencies of the different "orientation" contributing to the nutation signal even for a narrow orientation selection given by the resonance magnetic field. Besides that, the use of a relatively large sample (*ca.* 1 cm length, to compensate the low intensity of the EPR signal due to dilution) results in an inhomogeneity of the microwave magnetic field intensity, B_1, and thus an additional distribution of the nutation frequencies. The dephasing due to the distribution of frequencies is the reason of the shortening of the decay time of the observed nutation signal, which means the observed decay time is not a good estimation of T_R, the actual relaxation time of the nutation.

Supporting Information

Supporting Information is available from the Wiley Online Library or from the author. IR and additional UV-Vis spectroscopy, mass spectrometry, crystallographic details, relevant structural parameters and additional structures views, powder XRD data, complete *ac* susceptibility data, complete EPR data and data analysis, Langmuir isotherms, TEM images and analysis, additional AFM and XPS data (PDF)

Acknowledgements

Authors acknowledge funding from the Spanish MINECO through projects MAT2014-53961-R (OR, EN), MAT2015-70868-ERC (OR, AU), MAT2016-78257-R (IG, MAA), MAT2017-86826-R (OR, EN, AU) and CTQ2015-64486-R (PJA), as well as from the Aragón government (DGA, consolidated group PLATON E31_17R). MAA acknowledges the support of Spanish Ministerio de Educación for a FPU grant). The authors are grateful to Dr. G. Antorrena (LMA) for his help with XPS experiments. This research used resources of the

Advanced Light Source, which is a DOE Office of Science User Facility under contract no. DE-AC02-05CH11231.

References

[1] a) T. D. Ladd, F. Jelezko, R. Laflamme, Y. Nakamura, C. Monroe, J. L. OBrien, *Nature* **2010**, *464*, 45–53; b) M. A. Nielsen, I. L. Chuang, *Quantum Information and Quantum Computation*, Cambridge University Press, **2011**.

[2] see for example a) O. Mangold, A. Heidebrecht, M. Mehring, *Phys. Rev. A* **2004**, *70*, 042307; b) C. Negrevergne, T. S. Mahesh, C. A. Ryan, M. Ditty, F. Cyr-Racine, W. Power, N. Boulant, T. Havel, D. G. Cory, R. Laflamme, *Phys. Rev. Lett.* **2006**, *96*, 170501; c) S. Nakazawa, S. Nishida, T. Ise, T. Yoshino, N. Mori, R. D. Rahimi, K. Sato, Y. Morita, K. Toyota, D. Shiomi, M. Kitagawa, H. Hara, P. Carl, P. Höfer, T. Takui, *Angew. Chem. Int. Ed.* **2012**, *51*, 9860-9864 and references therein.

[3] a) M. N. Leuenberger, D. Loss, *Nature* **2001**, *410*, 789-793; b) F. Troiani, A. Ghirri, M. Affronte, S. Carretta, P. Santini, G. Amoretti, S. Piligkos, G. Timco, R. E. P. Winpenny, *Phys. Rev. Lett.* **2005**, *94*, 207208; c) A. Ardavan, O. Rival, J. Morton, S. Blundell, A. Tyryshkin, G. Timco, R. E. P. Winpenny, *Phys. Rev. Lett.* **2007**, *98*, 057201.

[4] a) C. G. Wedge, G. A. Timco, E. T. Spielberg, R. E. George, F. Tuna, S. Rigby, E. J. L. McInnes, R. E. P. Winpenny, *Phys. Rev. Lett.* **2012**, *108*, 107204; b) K. Bader, D. Dengler, J. van Slageren, *Nat. Commun.* **2015**, *5*, 5304; c) J. M. Zadrozny, J. Niklas, O. G. Poluektov, D. E. Freedman, *Cent. Sci.* **2015**, *1*, 488–492; d) M. Atzori, L. Tesi, E. Morra, M. Chiesa, L. Sorace, R. Sessoli, *J. Am. Chem. Soc.* **2016**, *138*, 2154–2157.

[5] a) F. Luis, A. Repollés, M. J. Martínez-Pérez, D. Aguilà, O. Roubeau, D. Zueco, P. J. Alonso, M. Evangelisti, A. Camón, J. Sesé, L. A. Barrios, G. Aromí, *Phys. Rev. Lett.* **2011**,

107, 117203; b) G. Aromí, A. Aguilà, P. Gamez, F. Luis, O Roubeau *Chem. Soc. Rev.* **2012**, *41*, 537–546; c) D. Aguilà, L. A. Barrios, V. Velasco, O. Roubeau, A. Repollés, P. J. Alonso, J. Sesé, S. J. Teat, F Luis, G. Aromí, *J. Am. Chem. Soc.* **2014**, *136*, 14215–14222; d) A. Ardavan, A. M. Bowen, A. Fernandez, A. J. Fielding, D. Kaminski, F. Moro, C. A. Muryn, M. D. Wise, A. Ruggi, E. J. L. McInnes, K. Severin, G. A. Timco, C. R. Timmel, F. Tuna, G. F. S. Whitehead, R. E. P. Winpenny, *npj Quantum Information* **2015**, *1*, 15012; e) J. Ferrando-Soria, E. M. Pineda, A. Chiesa, A. Fernandez, S. A. Magee, S. Carretta, P. Santini, I. J. Vitorica-Yrezabal, F. Tuna, G. A. Timco, E. J. L. McInnes, R. E. P. Winpenny, *Nat. Commun.* **2016**, *7*, 11377.

[6] C. Godfrin, A. Ferhat, R. Ballou, S. Klyatskaya, M. Ruben, W. Wernsdorfer, F. Balestro, *Phys. Rev. Lett.* **2017**, *119*, 187702.

[7] R. J. Schoelkopf, S. M. Girvin, *Nature* **2008**, *451*, 664–669.

[8] M. D. Jenkins, D. Zueco, O. Roubeau, G. Aromí, J. Majer, F. Luis, *Dalton Trans.* **2016**, *45*, 16682–16693.

[9] a) M. Jenkins, T. Hümmer, M. J. Martínez-Pérez, J. García-Ripoll, D. Zueco, F. Luis, *New J. Phys.* **2013**, *15*, 095007; b) A. Ghirri, C. Bonizzoni, F. Troiani, N Buccheri, L. Beverina, A. Cassinese, M. Affronte, *Phys. Rev. A* **2016**, *93*, 063855; c) M. Mergenthaler, J. Liu, J. J. Le Roy, N. Ares, A. L. Thompson, L. Bogani, F. Luis, S. J. Blundell, T. Lancaster, A. Ardavan, G. A. D. Briggs, P. J. Leek, E. A. Laird, *Phys. Rev. Lett.* **2017**, *119*, 147701; d) C. Bonizzoni, A. Ghirri, M. Affronte, *Adv. Phys. X* **2018**, *3*, 1435305.

[10] a) D. Gatteschi, A. Cornia, M. Mannini, R. Sessoli, *Inorg. Chem.* **2009**, *48*, 3408–3419; b) A. Cornia, M. Mannini, P. Sainctavit, R. Sessoli, *Chem. Soc. Rev.* **2011**, *40*, 3076–3091; c) N. Domingo, E. Bellido, D. Ruiz-Molina, *Chem. Soc. Rev.* **2012**, *41*, 258–302.

[10] typical AFM / STM images of deposits of SMMs on various types of substrates and using various kinds of attachment systematically show inhomogeneous distribution and

therefore varying density and molecule···molecule separation. See numerous examples in refs. 9.

[12] the orientation of SMMs attached to gold could be determined but confirmed it is rather random and uncontrolled with the grafting strategies used. See M. Mannini, F. Pineider, C. Danieli, F. Totti, L. Sorace, P. Sainctavit, M.-A. Arrio, E. Otero, L. Joly, J. C. Cezar, A. Cornia, R. Sessoli, *Nature* **2010**, *468*, 417–421.

[13] K. Bader, M. Winkler, J. van Slageren, *Chem. Comm.* **2016**, *52*, 3623–3626.

[14] S. Huh, S-J. Kim, Y. Kim, *CrystEngComm* **2016**, *18*, 345–368.

[15] a) T. Sato, W. Mori, C. N. Kato, T. Ohmura, T. Sato, K. Yokoyama, S. Takamizawa, S. Naito, *Chem. Lett.* **2003**, *32*, 854–855; b) E-Y. Choi, C. A. Wray, C. Hub, W. Choe, *CrystEngComm* **2009**, *11*, 553–555; c) R. Makiura, R. Usui, E. Phol, K. Prassides, *Chem. Lett.* **2014**, *43*, 1161–1163.

[16] M. Zhao, Y. Wang, Q. Ma, Y. Huang, X. Zhang, J. Ping, Z. Zhang, Q. Lu, Y. Yu, H. Xu, Y. Zhao, H. Zhang, *Adv. Mater.* **2015**, *27*, 7372-7378.

[17] a) R. Makiura, S. Motoyama, Y Umemura, H. Yamanaka, O. Sakata, H Kitagawa, *Nature Mater.* **2010**, *9*, 565–571; b) S. Motoyama, R. Makiura, O. Sakata, H. Kitagawa, *J. Am. Chem. Soc.* **2011**, *133*, 5640–5641.

[18] R. Makiura, O. Konovalov, *Sci. Rep.* **2013**, *3*, 2506

[19] R. Makiura, K. Tsuchiyama, O. Sakata, *Cryst. Eng. Comm*. **2011**, *13*, 5538–5541.

[20] R. Makiura, R. Usui, Y. Sakai, A. Nomoto, A. Ogawa, O. Sakata, A. Fujiwara, *ChemPlusChem* **2014**, *79*, 1352–1360.

[21] K. L. Cunningham, K. M. McNett, R. A. Pierce, K. A. Davis, H. H. Harris, D. M. Falck, D. R. McMillin, *Inorg. Chem.*, **1997**, *36*, 608–613.

[22] see for instance P. J. Alonso, *"Electron paramagnetic resonance of paramagnetic metallomesogens"* in *Metallomesogens. Synthesis, Properties and applications*, ed. J. L. Serrano. VCH, Weinheim, 1996, ch. 9.

[23] a) A. Abragam, B. Bleaney, *Electron Paramagnetic Resonance of Transition Ions*, Dover, New York, **1986**; b) S. K. Hoffmann, W. Hilczer, J. Goslar, M. M. Massa, R. Calvo, *J. Magn. Reson.*, **2001**, *153*, 92–102.

[24] R. Orbach, R. *Proc. R. Soc. A Math. Phys. Eng. Sci.*, **1961**, *264*, 485–495.

[25] G. Ablart, J. Pescia, *Phys. Rev. B*, **1980**, *22*, 1150–1162.

[26] A. C. de Vroomen, E. E. Lijphart, N. J. Poulis, *Physica*, **1970**, *47*, 458–484.

[27] S. Gómez-Coca, A. Urtizberea, E. Cremades, P. J. Alonso, A. Camón, E. Ruiz, F. Luis, *Nat. Commun.*, **2014**, *5*, 4300.

[28] J. Soeteman, A. J. van Duyneveldt, C. L. M. Pouw, W. Breur, *Physica*, **1973**, *66*, 63–69.

[29] L. Escalera-Moreno, N. Suaud, A. Gaita-Ariño, E. Coronado, *J. Phys. Chem. Lett.* **2017**, *8*, 1695–1700.

[30] a) L. Tesi, A. Lunghi, M. Atzori, E. Lucaccini, L. Sorace, F. Totti, R. Sessoli, *Dalton Trans.* **2016**, *45*, 16635-16643; b) M. Atzori, S. Benci, E. Morra, L. Tesi, M. Chiesa, R. Torre, L. Sorace, R. Sessoli, *Inorg. Chem.* **2018**, *57*, 731-740.

[31] L. Tesi, E. Lucaccini, I. Cimatti, M Perfetti, M. Mannini, M. Atzori, E. Morra, M. Chiesa, A. Caneschi, L. Sorace, R. Sessoli, *Chem. Sci.*, **2016**, *7*, 2074-2083.

[32] A. Schweiger, G. Jeschke, *Principles of pulse electron paramagnetic resonance*, Oxford University Press, NY, 2001, ch. 8.

[33] note that the expression used differs from the conventional expression for a stretched exponential dependence given by $y(t_d) = y_\infty - y_0 e^{-(t_d/T_1')^\beta}$, which is equivalent to our expression with $T_1 = T'_1/\beta$. In the case where the stretched exponential represents a distribution of exponential decays, it has been proven that for $\beta \leq 1$ T_1 corresponds to the mean value of the relaxation times, see ref. 34.

[34] D. C. Johnston, *Phys. Rev. B*, **2006**, *74*, 184430.

[35] a) H. L. Flanagan, D. J. Singel, *J. Chem. Phys.* **1988**, *89*, 2585-2586; b) J. J. Shane, P. A. A. W. van der Heijden, E. J. Reijerse, E. de Boer, *Appl. Mag. Reson.* **1994**, *6*, 427-454.

[36] For this, a density of 0.495 [Cu(TCPP)] per nm^3 is estimated for the deposited [Cu(TCPP)Zn_2] sheets, considering a sheet thickness of 0.7 nm and the in-plane structure derived from GIXS, which results in an equivalent concentration of 0.821 mol L^{-1}. We then use the molar attenuation coefficient of the [Cu(H_4TCPP)] molecule derived from the maximum absorption of the Soret band in Fig. S4 (478793 $Lmol^{-1}cm^{-1}$), and assume the porphyrin moieties are flat within the [{Cu(TCPP)}Zn_2] deposit, i.e. the angle of all transition moments form a 90º angle with the surface. See Ref. 37 for more details.

[37] T. Hasegawa, Y. Ushiroda, M. Kawaguchi, Y. Kitazawa, M. Nishiyama, A. Hiraoka, J. Nishijo, *Langmuir*, **1996**, *12*, 1566–1571.

[38] M. D. Jenkins, U. Naether, M. Ciria, J. Sesé, A. J. Atkinson, C. Sánchez-Azqueta, E. Del Barco, J. Majer, D. Zueco, F. Luis, *Appl. Phys. Lett.*, **2014**, *105*, 162601.

[39] R. Makiura, H. Kitagawa, Y. Akita, M. Yoshimoto, *J. Colloid Interface Sci.*, **2014**, *413*, 71–77.

[40] E. Bellido, P. González-Monje, A. Repollés, M. Jenkins, J. Sesé, D. Drung, T. Schurig, K. Awaga, F. Luis, D. Ruiz-Molina, *Nanoscale*, **2013**, *5*, 12565–12573.

[41] P. Manandhar, K-S. Chen, K. Aledealat, G. Mihajlović, C. S. Yun, M. Field, G. J. Sullivan, G. F. Strouse, P. B. Chase, S. von Molnár, P. Xiong, *Nanotechnology*, **2009**, *20*, 355501.

[42] C. Carbonell, K. C. Stylianou, J. Hernando, E. Evangelio, S. A. Barnett, S. Nettikadan, I. Imaz, D. Maspoch, *Nat. Commun.*, **2013**, *4*, 2173.

[43] J. M. Zadrozny, A. T. Gallagher, T. D. Harris, D. E. Freedman, *J. Am. Chem. Soc.*, **2017**, *139*, 7089–7094.

[44] SAINT v8.37a and SADABS–2014/5, Bruker AXS Inc., Madison, Wisconsin, USA.

[45] G. M. Sheldrick, CELL_NOW and TWINABS, Bruker AXS Inc., Madison, Wisconsin, USA.

[46] G. M. Sheldrick, *Acta Cryst. A* **2015**, *71*, 3–8.

[47] G. M. Sheldrick, *Acta Cryst. C* **2015**, *71*, 3–8.

[48] G. Ciatto, M. H. Chu, P. Fontaine, N. Aubert, H. Renevier, J. L. Deschanvres, *Thin Solid Films*, **2016**, *617*, 48–54.